

Open-geometry Fourier modal method: modeling nanophotonic structures in infinite domains

TEPPO HÄYRYNEN,* JAKOB ROSENKRANTZ DE LASSON, AND NIELS GREGERSEN

DTU Fotonik, Department of Photonics Engineering, Technical University of Denmark, Ørstedes Plads, Building 343, DK-2800 Kongens Lyngby, Denmark

*Corresponding author: tepha@fotonik.dtu.dk

Received 10 March 2016; revised 10 May 2016; accepted 25 May 2016; posted 25 May 2016 (Doc. ID 260947); published 9 June 2016

We present an open-geometry Fourier modal method based on a new combination of open boundary conditions and an efficient k -space discretization. The open boundary of the computational domain is obtained using basis functions that expand the whole space, and the integrals subsequently appearing due to the continuous nature of the radiation modes are handled using a discretization based on nonuniform sampling of the k space. We apply the method to a variety of photonic structures and demonstrate that our method leads to significantly improved convergence with respect to the number of degrees of freedom, which may pave the way for more accurate and efficient modeling of open nanophotonic structures. © 2016 Optical Society of America

OCIS codes: (050.1755) Computational electromagnetic methods; (350.3950) Micro-optics; (230.7370) Waveguides; (000.3860) Mathematical methods in physics; (000.4430) Numerical approximation and analysis.

<http://dx.doi.org/10.1364/JOSAA.33.001298>

1. INTRODUCTION

Many important properties of photonic structures such as cavities [1] and waveguides [2,3] depend on the radiative losses that stem from coupling of energy into freely propagating optical modes that escape the system. The quality, or Q , factor of photonic resonators as well as the spontaneous emission (SE) β factor in waveguides are important figures of merit in the analysis of nanolasers [4] and single-photon sources [5], for example, and these quantities depend sensitively on the radiative losses. In modeling such open photonic systems, the choice of boundary conditions (BCs) at the computational domain edges becomes crucial and may impact the results not just quantitatively but also qualitatively. Integral equation Green's function formulations inherently adopt this openness [6], while for numerical techniques relying on finite-sized computational domains like the finite-difference time-domain method [7] and the finite element method [8], this is achieved using artificial absorbing boundaries, typically in the form of so-called perfectly matched layers (PMLs) [9].

In Fourier-based modal-expansion techniques [10,11], PMLs can be implemented using complex coordinate transforms [12]. The absorbing boundaries are implemented by mapping the real spatial coordinates into complex ones, which is straightforward to implement. However, it is unclear which complex coordinate transform to implement and why, and there have been no systematic studies on the influence of PML parameters and the size of the computational domain on computed quantities of interest. In addition to Fourier

resolution convergence checks, the size of the computational domain should be varied to estimate the computational accuracy, but this is rarely done [13–15]. In our experience, different choices of PML parameters and domain sizes lead to results that agree qualitatively, but may vary substantially—for example, errors of Q factors $\sim 20\%$ [13] and errors of dipole coupling to radiation modes $\sim 15\text{--}25\%$ [16] have been reported.

Instead of searching an extremely large PML parameter space without intuitive or clear guidelines, we propose a different technique that relies on finite-sized structures and open BCs, with fields expanded via Fourier *integrals* instead of Fourier *series*. The use of Fourier integrals, in principle, gives an exact description but, for numerical implementation, a k -space discretization is required that we, however, have the freedom to choose. Similar ideas have previously been reported for two-dimensional (2D) [17] and rotationally symmetric three-dimensional (3D) [18–20] structures, but without discussion of the important problem of choosing the k -space discretization. Furthermore, the important example of dipole emission, which depends sensitively on the proper implementation of the open BCs, was not treated in these works. In this paper, we address both these central issues. Our examples include calculations of light emission from emitters placed in rotationally symmetric waveguides [21] and reflection of the fundamental mode from a waveguide–metal interface [22]. We term this new approach an open-geometry Fourier modal method (oFMM).

This paper is organized as follows. Section 2 outlines the theory of the oFMM approach, while the details are given in Appendix A. The details of the new discretization scheme are discussed in Section 3. The method is tested for several structures by calculating dipole emission rates, β factors, and modal reflection coefficients in Section 4. Finally, Section 5 concludes the work.

2. THEORY

In this section, we outline the derivation of the open BC formalism and introduce the theoretical concepts required to understand the results of the following sections. The detailed derivations of the open BC formalisms in rotationally symmetric geometry are given in Appendix A.

A. Open Boundary Condition Formalism

We employ the open BC formalism to describe the electromagnetic field propagation in rotationally symmetric structures. Complete vectorial description is used in connection with Fourier expansion to describe the Maxwell's equations in a z -invariant material section. Using cylindrical coordinates in the rotationally symmetric case allows for simplification of the problem to 1D expansion in the radial coordinate. The z dependence is treated by combining z -invariant sections using the scattering matrix formalism (see, e.g., [23] and [24] for details). Our task is then to determine the lateral electric and magnetic field components of the eigenmodes, which are subsequently used as an expansion basis for the optical field. In the conventional FMM, this is done by expanding the field components as well as the permittivity $\epsilon(\mathbf{r}_\perp)$ and $\eta(\mathbf{r}_\perp) \equiv 1/\epsilon(\mathbf{r}_\perp)$ in Fourier series in the lateral coordinates \mathbf{r}_\perp on a *finite-sized* computational domain, implying that these functions vary *periodically* in these coordinates. In the open boundary formalism, we instead consider an *infinite-sized* computational domain and employ expansions in Fourier *integrals*. Essentially, any expansion basis can be used, e.g., the plane wave basis in the general 3D case. However, in rotationally symmetric structures, we use the Bessel J function basis since it leads to reduced dimensionality of the problem [18]. In the following, we describe the general steps and equations required to expand the field components and to solve for the expansion and propagation coefficients. The specific equations and derivations are given in Appendix A and referenced throughout this section.

Starting from the time-harmonic Maxwell's equations $\nabla \times \mathbf{E}(\mathbf{r}) = i\omega\mu_0\mathbf{H}(\mathbf{r})$ and $\nabla \times \mathbf{H}(\mathbf{r}) = -i\omega\epsilon(\mathbf{r})\mathbf{E}(\mathbf{r})$ [written using cylindrical coordinates in Eqs. (A1)–(A6) in Appendix A], where ϵ is the permittivity of the medium, μ_0 is the vacuum permeability, ω is the angular frequency, and \mathbf{E} and \mathbf{H} are the electric and magnetic fields, we obtain

$$\nabla \times [\nabla \times \mathbf{E}(\mathbf{r})] = \omega^2\mu_0\epsilon(\mathbf{r})\mathbf{E}(\mathbf{r}), \quad (1)$$

which is given in cylindrical coordinates in Eqs. (A7)–(A9). The fields in the single z -invariant section can be expanded using the eigenmodes of the system as

$$\begin{aligned} \mathbf{E}(\mathbf{r}_\perp, z) = & \sum_j a_j \mathbf{E}_j(\mathbf{r}_\perp) \exp(\pm i\beta_j z) \\ & + \int a(k) \mathbf{E}(k, \mathbf{r}_\perp) \exp(\pm i\beta(k)z) dk, \end{aligned} \quad (2)$$

where β_j and $\beta(k)$ denote the propagation constants that in general admit no closed-form expression and are thus determined numerically, and a_j and $a(k)$ denote the weights of the corresponding modes. Furthermore, the summation index j denotes all the guided modes, while the integral accounts for the radiation and evanescent modes. In numerical simulations, the continuous integral is approximated by a sum as

$$\begin{aligned} & \int a(k) \mathbf{E}(k, \mathbf{r}_\perp) \exp(\pm i\beta(k)z) dk \\ & \approx \sum_l a_l \mathbf{E}_l(k_l, \mathbf{r}_\perp) \exp(\pm i\beta_l z) \Delta k_l, \end{aligned} \quad (3)$$

where $\Delta k_l = k_l - k_{l-1}$ and $k_l = \sqrt{(nk_0)^2 - \beta_l^2}$, with k_0 denoting the wavenumber in vacuum and n being the refractive index of the material. Similar equations hold for the magnetic field.

Using the discretized eigenfunction expansion in Eqs. (2) and (3), the fields in each z -invariant section can be expressed with column vectors \mathbf{a} consisting of electric and magnetic field expansion coefficients, $[a_j, a_l \Delta k_l]^T$, all denoted with the single index j in the following. Thus, taking the z derivative of Eq. (2), we can formulate an eigenvalue problem describing the fields in the system as

$$\mathbf{M}\mathbf{a} = i\beta\mathbf{a}, \quad (4)$$

where the elements of matrix \mathbf{M} are obtained by expanding the eigenfunction on a Fourier–Bessel basis in rotationally symmetric geometry as discussed subsequently.

Since the eigenfunctions are specific to each layer, we choose a general basis and expand the eigenfunctions in each layer using the common basis. Thus, any function (the field components and the relative permittivity) can be expanded as a Fourier transform

$$f(\mathbf{r}_\perp) = \int_{k_\perp} c_f(k_\perp) g(k_\perp, \mathbf{r}_\perp) dk_\perp, \quad (5)$$

where k_\perp is the transverse wavenumber while $c_f(k_\perp)$ and $g(k_\perp, \mathbf{r}_\perp)$ are the expansion coefficients and the basis functions, respectively. In the rotationally symmetric case, $k_\perp = k_r$, $\mathbf{r}_\perp = r$, and the basis functions $g(k_r, r)$ are the Bessel J -functions [cf. Eqs. (A15) and (A16)]. While in the analytical definition of the Fourier transform the expansion basis in Eq. (5) is infinite, for the numerical calculations the basis must be truncated as

$$\int_{k_\perp} c_f(k_\perp) g(k_\perp, \mathbf{r}_\perp) dk_\perp \simeq \sum_{m=1}^M c_f(k_{\perp,m}) g(k_{\perp,m}, \mathbf{r}_\perp) \Delta k_{\perp,m}, \quad (6)$$

where the discretization steps $\Delta k_{\perp,m}$ will be a function of the index m in the generalized approach, as will be discussed in Section 3. This is in contrast to previous approaches [17,18], and we show later that such a nonuniform discretization is a significant improvement. The expansions in the cylindrical coordinate system are given by Eqs. (A15)–(A16). Furthermore, the elements of \mathbf{M} are given in Eqs. (A23)–(A26). Solving for the eigenvectors and eigenvalues of matrix \mathbf{M} yields the expansion coefficients and propagation constants in the z -invariant structures, while the fields in the full structure are then obtained by combining the z -invariant sections using the scattering matrix formalism.

B. Dipole Emission

The field emitted by a point dipole placed at \mathbf{r}_{pd} inside a z -invariant structure can be represented as

$$\begin{aligned} \mathbf{E}(\mathbf{r}) &= \sum_j a_j(\mathbf{r}_{\text{pd}}, \mathbf{p}) \mathbf{E}_j(\mathbf{r}) \\ &= \sum_j \sum_m a_j c_{j,m} \mathbf{g}_m(\mathbf{r}) \Delta k_{\perp,m} e^{\pm i\beta_j(z-z_{\text{pd}})}, \end{aligned} \quad (7)$$

where $\mathbf{E}_j(\mathbf{r})$ is the electric field of j th eigenmode and $a_j(\mathbf{r}_{\text{pd}}, \mathbf{p})$ is the dipole coupling coefficient to mode j , which can be calculated using the Lorentz reciprocity theorem [24]. The coupling coefficient depends on the dipole position \mathbf{r}_{pd} and dipole moment \mathbf{p} through a dot-product $\mathbf{p} \cdot \mathbf{E}_j(\mathbf{r}_{\text{pd}})$. For the sake of notational clarity, we omit these dependencies in the following. Furthermore, $c_{j,m}$ are the expansion coefficients for mode j , and $\mathbf{g}_m(\mathbf{r}_{\perp})$ are the basis functions.

The emitted field [Eq. (7)] consists of three contributions [25]: guided modes, radiation modes, and evanescent modes. In a waveguide surrounded by air, the modes are guided if the propagation constant β_j obeys $k_0^2 < \beta_j^2 \leq (n_w k_0)^2$, where n_w is the refractive index of the waveguide. In contrast, the modes are radiating if $0 < \beta_j^2 \leq k_0^2$ and evanescent if $\beta_j^2 < 0$. We will apply this classification in Section 3 when we investigate discretization schemes.

The normalized power emitted by dipole to a selected mode can be expressed as [24,26]

$$\frac{P_j}{P_{\text{Bulk}}} = \frac{\text{Im}\{a_j \mathbf{E}_j(\mathbf{r}_{\text{pd}})\}}{P_{\text{Bulk}}} = \frac{\text{Im}\{\sum_m a_j c_{j,m} \mathbf{g}_m(\mathbf{r}_{\text{pd}}) \Delta k_{\perp,m}\}}{P_{\text{Bulk}}}, \quad (8)$$

where P_{Bulk} is the emitted power in a bulk medium. The normalized emitted power is equal to the normalized emission rate [26] $\gamma_j/\gamma_{\text{Bulk}} = P_j/P_{\text{Bulk}}$, where γ_j and γ_{Bulk} are the emission rates to mode j and in a bulk medium, respectively. In the following, we will use only the normalized unitless quantity $\Gamma_j = \gamma_j/\gamma_{\text{Bulk}}$ for the emission rate. Thus, the spontaneous emission factor (i.e., the β factor), defined as the ratio of emission to the fundamental mode (FM) and the total emission [21], is obtained as

$$\beta = \frac{a_{\text{FM}} \mathbf{E}_{\text{FM}}(\mathbf{r}_{\text{pd}})}{\sum_j a_j \mathbf{E}_j(\mathbf{r}_{\text{pd}})} = \frac{a_{\text{FM}} \sum_m c_{\text{FM},m} \mathbf{g}_m(\mathbf{r}_{\text{pd}}) \Delta k_{\perp,m}}{\sum_j \sum_m a_j c_{j,m} \mathbf{g}_m(\mathbf{r}_{\text{pd}}) \Delta k_{\perp,m}}. \quad (9)$$

3. DISCRETIZATION SCHEME

In addition to the open BCs described in the previous section, an advantage of the presented method is that it enables the use of a nonuniform k -space discretization, which allows for a high cut-off value together with dense-sampling k -space regions while still maintaining a moderate total number of modes, i.e., achieving the required accuracy with less computational power. In this section, we investigate how to select the cut-off value $k_{\text{cut-off}}$ and how to sample the k space effectively. The numerical tests in Section 4 show that faster convergence is achieved using an appropriate mode-sampling scheme.

The transverse wavenumber values in the conventional modal expansion approach [10] are selected equidistantly:

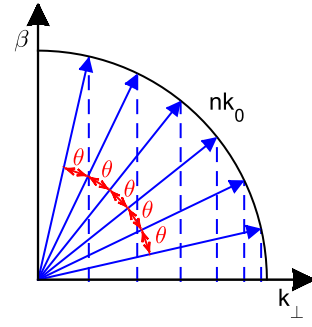


Fig. 1. Nonuniform discretization scheme: in a bulk medium, all propagation directions have equal weights. Therefore, the wavevector \mathbf{k} is sampled in the $(\beta, \mathbf{k}_{\perp})$ plane using equidistant angles, as shown by θ in the figure. Due to the uniform angle distribution, the k_{\perp} discretization is more dense close to nk_0 .

$$k_m = m\Delta k = \frac{m}{M+1} k_{\text{cut-off}}, \quad (10)$$

where $m = 1, \dots, M$ and the discretization step size depends on the selected cut-off value $k_{\text{cut-off}}$ and number of modes M as $\Delta k = k_{\text{cut-off}}/(M+1)$.

In a bulk medium, light emission occurs with equal weights in all directions. Therefore, a natural starting point for the discretization scheme is to sample the wavevectors in the $(\beta, \mathbf{k}_{\perp})$ plane with equidistant angles [27], as shown in Fig. 1. This is also known as the Chebyshev grid [28]. Then the different transverse wavenumber values are given by $k_m = nk_0 \sin(\theta_m)$, where the equidistantly sampled angles $0 < \theta_m < \pi/2$ are measured from the β axis. Although the values of θ_m are selected uniformly, the values of k_m are more densely sampled in the proximity of nk_0 , cf. Fig. 1. If, instead of a bulk medium, we consider a structure like a nanowire consisting of several materials, it is necessary also to account for the modes beyond nk_0 .

To obtain insight into the discretization in different types of structures, we first investigate emission from a radially oriented point dipole placed on the axis of rotationally symmetric infinite semiconductor nanowires having radius from subwavelength to several wavelengths and a refractive index n_w (see Fig 2). The radial component of the emitted electric field $E_r(r) = \sum_j a_j E_{r,j}(r) = \sum_j a_j \sum_m c_{m,j} \mathbf{g}_{r,m}(r) \Delta k_m$ can be written by rearranging the terms as follows [cf. Section 2.B, Eqs. (6) and (7), and Appendix A]:

$$E_r(r) = i \sum_m \left[\sum_{j=\text{g.m.}} a_j \mathcal{E}_{j,m}(r) + \sum_{j=\text{r.m.}} a_j \mathcal{E}_{j,m}(r) \right] k_m \Delta k_m, \quad (11)$$

where a shorthand notation $\mathcal{E}_{j,m}(r) = b_{n,m,j}^E J_{n+1}(k_m r) - c_{n,m,j}^E J_{n-1}(k_m r)$ has been used for the radial component of the electric field defined in Eq. (A15). The sum over j describes the modes of the structure, while index m accounts for the expansion of the modes using the selected basis functions. The first summation inside the brackets in Eq. (11) describes the guided-mode ($k_0^2 < \beta_j^2 \leq (n_w k_0)^2$) contribution, while the second summation describes the radiation mode ($0 < \beta_j^2 \leq k_0^2$) contribution to the total emission with radial wavenumber k_m . Figure 2 shows the guided and radiation mode contributions

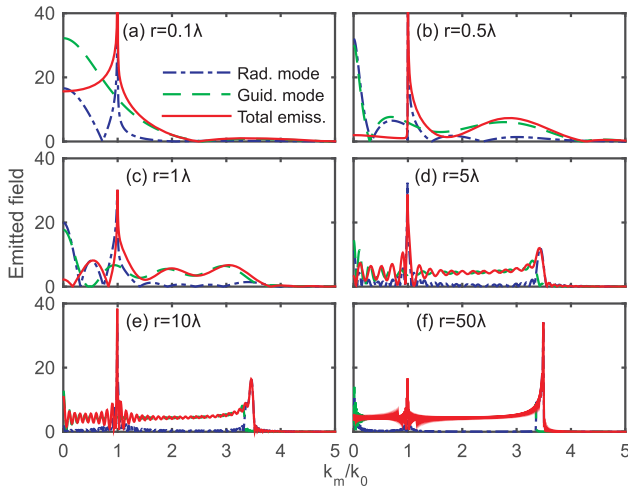


Fig. 2. Fourier components of a point dipole emission defined in Eq. (11). The figures show the calculated radiation and guided mode contributions and the total emission as function of the radial wave number in z -invariant nanowires of varying radii. The nanowire has a refractive index of $n_w = 3.5$ and the wavelength is $\lambda = 950$ nm. An equidistant k discretization with 1500 points and $k_{\max} = 10k_0$ was used.

and their sum as functions of radial wavenumber. The emitted electric field has a peak around $k_m = k_0$. When the radius increases, a peak around $k_m = n_w k_0$ also gradually builds up, while in the bulk limit ($r/\lambda \gg 1$), the peak around k_0 disappears. These results indicate that (i) for wires with radius $r \lesssim \lambda$, the k space should be densely sampled around k_0 ; (ii) for wider structures, dense sampling around $n_w k_0$ is also required; while (iii) in bulk media, dense sampling is required only around $n_w k_0$. Thus, since we are mainly interested in the region where the wire radius is of the order of or smaller than the wavelength, we will use the following discretization scheme that is dense and symmetric around k_0 and where the discretization step-size gradually increases toward the cut-off value. Let M_1, M_2, M_3 be the fixed number of k values on the intervals $(0, k_0)$, $(k_0, 2k_0)$, and $(2k_0, k_{\text{cut-off}})$, respectively. Then we can write

$$\begin{aligned} k_m^{(1)} &= k_0 \sin(\theta_m), \quad \theta_m = \frac{\pi}{2M_1+1} m, \quad m = 1, \dots, M_1, \\ k_m^{(2)} &= k_0[2 - \sin(\theta_m)], \quad \theta_m = \frac{\pi}{2} \left(1 + \frac{m}{M_2+1}\right), \quad m = 1, \dots, M_2, \\ k_m^{(3)} &= k_{n_2}^{(2)} + \delta_1 m + \frac{\delta_2}{2} m(m+1), \quad m = 1, \dots, M_3, \end{aligned} \quad (12)$$

where we use a symmetric dense sampling around k_0 by setting $M_2 = M_1$. Furthermore, $\delta_1 = \Delta k_{M_2}^{(2)}$ is the biggest step size in the symmetric region and $\delta_2 = 2[k_{\text{cut-off}} - k_{M_2}^{(2)} - M_3 \delta_1]/[M_3(M_3 + 1)]$. When modeling bulk materials, k_0 will be multiplied with the refractive index as concluded above. In the following, we will use $M_1 = M_2 = M_3 = M/3$. The optimal values of M_i may vary depending on the geometry, but this choice limits the number of free parameters to the total number of modes M and to the cut-off value $k_{\text{cut-off}}$. Our examples will show that this selection leads to faster convergence

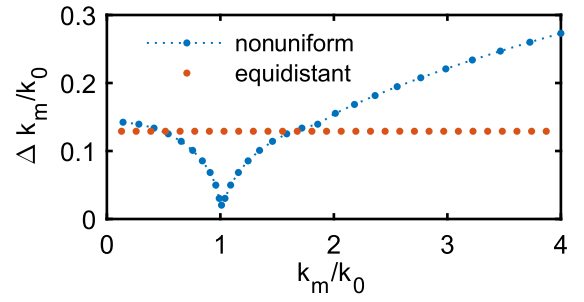


Fig. 3. Example of discretization step sizes Δk_m for a nonuniform discretization with $M_1 = M_2 = M_3 = 10$ and $k_{\text{cut-off}}/k_0 = 4$. For comparison, the equidistant discretization is also shown with the corresponding number of modes and cut-off values.

of the calculations than when using the equidistant discretization scheme. An example of a nonuniform discretization and a comparison to equidistant discretization are shown in Fig. 3.

In the next section, we use these discretization schemes in the modeling of various structures and compare the convergence and required computational power with those obtained using a conventional discretization scheme. When comparing the different discretization schemes, we use the same cut-off value and the same number of modes for both of the schemes.

4. RESULTS AND DISCUSSION

Next, after introducing the principles of the open BC formalism together with the new discretization strategy, we are ready to test the method with several numerical examples. The purpose of these selected examples is to show that the calculations using oFMM formalism converge toward a well-defined open-geometry limit and that faster convergence can be achieved using the discretization schemes introduced in Section 3 compared to using the conventional equidistant discretization. We start with calculating the dipole emission rates (or emission power) in a bulk medium and close to an interface, since these results can be verified analytically. After these basic checks, we investigate the performance of our method for the cases of light emission from emitters in waveguides as well as the case of reflection at a waveguide–metal interface, all of which depend critically on a correct and accurate description of the open boundaries.

A. Dipole Emission in Bulk and Close to an Interface

As a first example, we consider dipole emission in a bulk medium and close to a bulk–bulk interface. Both of these examples can also be solved analytically [26,29], allowing easy comparison of the convergence of the results. Figure 4(a) shows the dipole emission power in a bulk material ($n_b = 1$) calculated using the rotationally symmetric model and normalized with the analytical result. Numerical results are calculated using both the equidistant discretization and the nonuniform discretization presented in Section 3. The obtained results show that applying the nonuniform discretization leads to much faster convergence of the emission rates.

In the bulk medium case, only propagating modes contribute to the light emission, and the emission rate converges

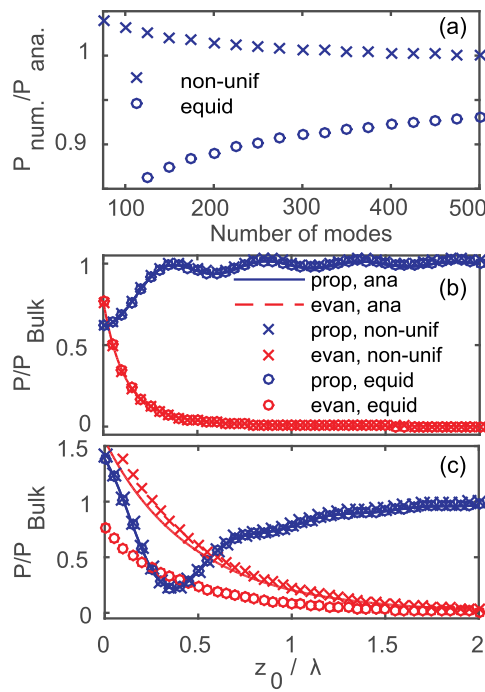


Fig. 4. (a) Calculated emission power P_{num} in a bulk medium ($n_b = 1$) normalized with analytical result P_{ana} with a fixed wavelength $\lambda = 950$ nm. Both numerical schemes have the wavenumber cut-off value $n_b k_0$ in the bulk medium, and the horizontal axis shows the number of modes included in the calculations. (b) Normalized dipole emission power in air in front of a glass ($\epsilon = 2.25$) half-space. The dipole is parallel to the interface. (c) Normalized power emitted by point dipole placed in air close to an air-metal interface ($\epsilon = -41 + 2.5i$). The dipole is perpendicular to the interface. Numerical results in (b) and (c) are calculated using a cut-off value of $2k_0$ and 200 modes. The powers are normalized with the bulk medium value and the distance z_0 from the interface with the wavelength $\lambda = 950$ nm.

provided that enough propagating modes are included in the calculation. In contrast, in the case of a dipole emitter in close proximity to an interface, the evanescent modes also contribute through evanescent mode scattering at the interface and re-excitation of the propagating modes. As a next example, we therefore investigate the interface case.

Figure 4(b) shows the power emitted by a dipole close to an air-glass interface while Fig. 4(c) shows the power emitted by a dipole close to an air-metal interface. The values of the metal and glass permittivities are $\epsilon = -41 + 2.5i$ and $\epsilon = 2.25$, respectively. In contrast to the bulk medium case in Fig. 4(a) where the cut-off was $n_b k_0$ ($n_b = 1$), we now need to include the evanescent modes. Figures 4(b) and 4(c) show the separate contributions from propagating and evanescent modes to the emission rate. Again, the nonuniform discretization leads to faster convergence, especially for the contribution from the evanescent modes.

B. Dipole Emitter in a Rotationally Symmetric Waveguide

Next, we investigate the emission in waveguides by calculating the emission rates to selected modes and the spontaneous

emission factor β . In contrast to the bulk medium and interface cases investigated in the previous section, we face an additional computational challenge, which is to compute the radiation modes accurately. The waveguides considered in nanophotonics usually support only a few guided modes. However, the total emission rate and thus the β factor depend on emission to a continuum of radiation modes that can radiate light out of the waveguide. Calculating the radiation modes accurately requires more extensive calculations than the emission on bulk medium, as will be seen in the following examples.

Similar to the calculations represented in [21], we consider a dipole emitter oriented along the wire axis in an infinitely long nanowire with $n_w = 3.45$, surrounded by air. Figure 5(a) presents the β factor and the emission rates to the fundamental guided mode (HE_{11}), the second guided mode (EH_{11}), and the radiation modes, all normalized to the bulk medium emission rate (see Section 2.B) as functions of the nanowire diameter. While the rates calculated using both the equidistant and nonuniform discretization schemes with 1200 modes and a cut-off value $25k_0$ agree well qualitatively, discrepancies are observed in the emission rate to radiation modes. Figure 5(b) shows a convergence investigation of the emission rate to radiation modes. We fix the nanowire geometry by setting the diameter as 0.3λ , use both discretization schemes, and vary the cut-off value of the transverse wavenumber as well as the number of modes. The results show that only a slight improvement is achieved by increasing the cut-off from $20k_0$ to $25k_0$, while the results depend on the number of modes for small mode numbers and converge around 500. At high mode numbers and cut-off values, the results converge to the same value.

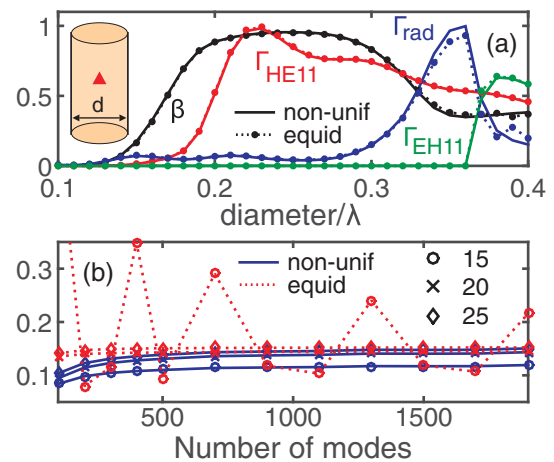


Fig. 5. Emission from a point dipole placed on the axis of an infinitely long rotationally symmetric nanowire of diameter d . (a) β factor and normalized emission rates to the first and second guided modes HE_{11} , EH_{11} and radiation modes as functions of d . The nanowire refractive index is $n = 3.45$ and the wavelength is $\lambda = 950$ nm. In both discretization schemes, 1200 modes and cut-off value of $25k_0$ were used. (b) The emission rate to radiation modes calculated with a fixed nanowire diameter 0.3λ . The horizontal axis shows the number of discretization modes, and the legend shows the cut-off value of the wavenumber in units of k_0 .

C. Reflection From Semiconductor Nanowire–Metal Interface

Finally, we investigate convergence of the method in a structure consisting of a nanowire standing on top of a metallic bulk layer. We calculate the reflection coefficient of the fundamental mode from a nanowire–metal interface similar to the setup investigated in [22]. The refractive indices of the nanowire and metal are $n_w = 3.5$ and $n_{\text{Ag}} = \sqrt{-41 + 2.5i}$ at the wavelength $\lambda = 950$ nm.

Figure 6 shows the calculated reflection coefficient as a function of the nanowire diameter using both (a) the equidistant sampling of the k_\perp discretization and (b) the nonuniform k_\perp discretization with several different numbers of discretization modes. In the nonuniform discretization, the k -space values are sampled more densely close to k_0 as discussed in Section 3. With small wire diameter, the reflection coefficients are essentially determined by the air–metal reflection ($R_{\text{Air-Ag}} \approx 0.98$) since in this limit the fundamental mode is mainly located in air. In contrast, in the limit of large nanowires, the fundamental mode is primarily located in the

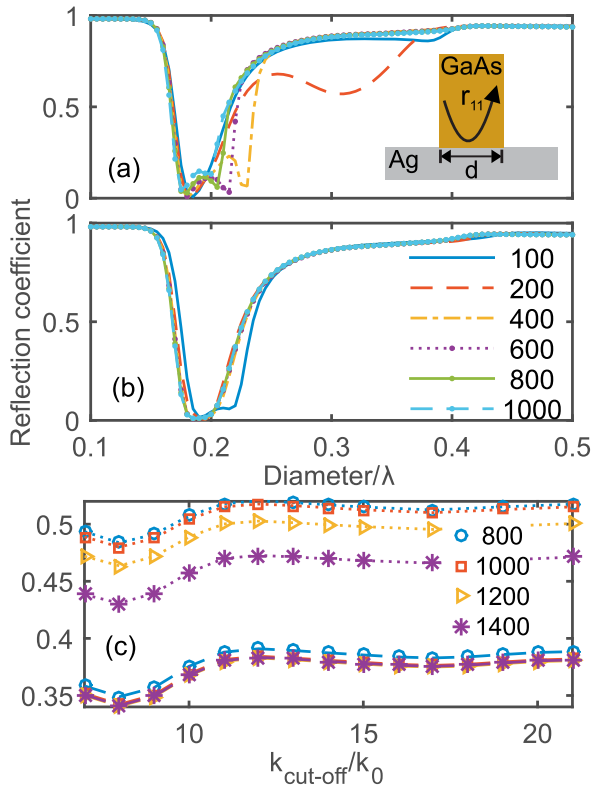


Fig. 6. Reflection coefficient of the fundamental mode calculated using (a) an equidistant grid and (b) a nonuniform grid with varying number of modes (shown in the legend) and $k_{\text{cut-off}} = 20k_0$ as a function of the nanowire diameter. The wire and the metal have refractive indices of $n_w = 3.5$ and $n_{\text{Ag}} = \sqrt{-41 + 2.5i}$, respectively, at wavelength $\lambda = 950$ nm. (c) The reflection coefficient of the fundamental mode using equidistant (dotted lines) and nonuniform (dashed lines) discretization and varying the cut-off of k_m for a nanowire having diameter of 0.22λ . The values of k_m are chosen such that k_m is equidistantly/nonuniformly sampled up to value $2n_w k_0$ ($n_w = 3.5$), with M shown in the legend. Then extra k_m values are added according to the scheme when the cut-off value is increased.

GaAs wire ($R_{\text{GaAs-Ag}} \approx 0.95$). Nevertheless, the figures show that faster convergence is obtained using the nonuniform discretization scheme instead of the equidistant k discretization scheme.

The reflection coefficients in Figs. 6(a) and 6(b) are obtained for a fixed cut-off value. Next, we fix the geometry and study the effect of the cut-off value of k_m . We select a wire having diameter of 0.22λ since the reflection coefficients shown in Figs. 6(a) and 6(b), calculated with different discretization schemes and with varying number of modes, have large variations around this diameter. Reflection coefficients as functions of the cut-off value calculated using both discretization schemes, with several different numbers of included modes, are shown in Fig. 6(c). The k_m values are chosen such that, when the cut-off is increased, extra points are added to the original k_m grid. The results show that the calculations converge around $5n_w k_0$.

The convergence checks in the selected waveguide examples represented in Figs. 5 and 6 show convergence for the investigated waveguide sizes and structures. Although these examples do not guarantee the convergence of our method in all waveguide sizes and geometries, we expect our method to converge in various types and sizes of waveguides provided that geometry-specific modifications to the discretization scheme are implemented.

5. CONCLUSIONS

We have demonstrated an open-geometry Fourier modal method formalism relying on open boundary conditions and nonuniform k -space sampling. Due to the inherent open boundary conditions, we avoid the artificial absorbing boundary conditions that in some cases lead to numerical artifacts. We have tested the approach by investigating the dipole emission in a bulk medium, close to an interface, and in waveguide structures, and by calculating the reflection coefficient of the fundamental waveguide mode for a nanowire–metal interface. Our simulations show that the calculations based on the open-geometry Fourier modal method formalism indeed converge toward an open geometry limit when varying the cut-off and the number of modes, and that the use of the nonuniform discretization scheme leads to a faster convergence of the simulations compared to using the conventional equidistant discretization. We expect that our new method will prove useful in the accurate modeling of a variety of nanophotonic structures, for which the open boundaries are inherently difficult to describe. Also, extension of the formalism to the three-dimensional Fourier modal method is straightforward and could be used for accurate modeling of, for example, light emission in photonic crystal membrane waveguides [2,3].

APPENDIX A: FOURIER-BESSEL EXPANSION IN CYLINDRICAL COORDINATES

The derivation of the open BC method in a rotationally symmetric case is outlined following the approach presented in [18]. We use cylindrical coordinates (r, ϕ, z) . Since the considered structures are rotationally symmetric, the angular dependence is expanded using Fourier series $\mathbf{E}(r, \phi, z) = \sum_{n=-\infty}^{\infty} \mathbf{E}_n(r, z) \exp(in\phi)$. The contributions $\mathbf{E}_n(r, z)$ for

different orders n are decoupled, and it is thus possible to solve for each order individually. This advantage is exploited to reduce the 2D lateral eigenvalue problem to an effective 1D problem.

Using the Fourier expansion, the time-harmonic Maxwell's equations $\nabla \times \mathbf{E}(\mathbf{r}) = i\omega\mu_0\mathbf{H}(\mathbf{r})$ and $\nabla \times \mathbf{H}(\mathbf{r}) = -i\omega\epsilon(\mathbf{r})\mathbf{E}(\mathbf{r})$ can be written component-wise as

$$\frac{\partial}{\partial z} E_{\phi,n} = \frac{in}{r} E_{z,n} - i\omega\mu_0 H_{r,n}, \quad (\text{A1})$$

$$\frac{\partial}{\partial z} E_{r,n} = \frac{\partial}{\partial r} E_{z,n} + i\omega\mu_0 H_{\phi,n}, \quad (\text{A2})$$

$$i\omega\mu_0 H_{z,n} = \frac{\partial E_{\phi,n}}{\partial r} + \frac{E_{\phi,n}}{r} - \frac{in}{r} E_{r,n}, \quad (\text{A3})$$

$$\frac{\partial H_{\phi,n}}{\partial z} = \frac{in}{r} H_{z,n} + i\omega\epsilon(r) E_{r,n}, \quad (\text{A4})$$

$$\frac{\partial H_{r,n}}{\partial z} = \frac{\partial H_{z,n}}{\partial r} - i\omega\epsilon(r) E_{\phi,n}, \quad (\text{A5})$$

$$-i\omega\epsilon(r) E_{z,n} = \frac{\partial H_{\phi,n}}{\partial r} + \frac{H_{\phi,n}}{r} - \frac{in}{r} H_{r,n}. \quad (\text{A6})$$

The Helmholtz equation for each Fourier component is given as $\Delta \mathbf{E}_n(r, z) \exp(in\phi) + \omega^2 \mu_0 \epsilon(r) \mathbf{E}_n(r, z) \exp(in\phi) = 0$, which, in component-wise form, reads as

$$\Delta E_{r,n} - \frac{E_{r,n}}{r^2} - \frac{2in}{r^2} E_{\phi,n} + \omega^2 \mu_0 \epsilon(r) E_{r,n} = 0, \quad (\text{A7})$$

$$\Delta E_{\phi,n} - \frac{E_{\phi,n}}{r^2} + \frac{2in}{r^2} E_{r,n} + \omega^2 \mu_0 \epsilon(r) E_{\phi,n} = 0, \quad (\text{A8})$$

$$\Delta E_z + \omega^2 \mu_0 \epsilon(r) E_z = 0. \quad (\text{A9})$$

Equations (A7) and (A8) are of the form of Bessel differential equations and couple the radial and angular components of the electric field. In order to simplify calculations, these equations are decoupled using the notation

$$E_n^\pm = E_{\phi,n} \pm iE_{r,n} \quad (\text{A10})$$

The transverse components of the Helmholtz equation can then be written as

$$\Delta E_n^+ - \frac{E_n^+}{r^2} + \frac{2n}{r^2} E_n^+ + \omega^2 \mu_0 \epsilon(r) E_n^+ = 0, \quad (\text{A11})$$

$$\Delta E_n^- - \frac{E_n^-}{r^2} - \frac{2n}{r^2} E_n^- + \omega^2 \mu_0 \epsilon(r) E_n^- = 0. \quad (\text{A12})$$

These Bessel-differential equations have general solutions

$$E_n^+ = E_{\phi,n} + iE_{r,n} = \int_{k_r=0}^{\infty} 2c_n^E(k_r, z) J_{n-1}(k_r r) k_r dk_r, \quad (\text{A13})$$

$$E_n^- = E_{\phi,n} - iE_{r,n} = \int_{k_r=0}^{\infty} 2b_n^E(k_r, z) J_{n+1}(k_r r) k_r dk_r, \quad (\text{A14})$$

where J_n is the Bessel function of the first kind having order of n . For numerical calculations, these Bessel integrals are

truncated as $\int_{k_r=0}^{\infty} k_r dk_r \rightarrow \sum_{m=1}^M k_m \Delta k_m$ and the Fourier series are truncated to $-N \leq n \leq N$. The expansions are

$$E_r(r, \phi, z) = i \sum_{n=-N}^N \sum_{m=1}^M k_m \Delta k_m [b_{n,m}^E(z) J_{n+1}(k_m r) - c_{n,m}^E(z) J_{n-1}(k_m r)] \exp(in\phi), \quad (\text{A15})$$

$$E_\phi(r, \phi, z) = \sum_{n=-N}^N \sum_{m=1}^M k_m \Delta k_m [b_{n,m}^E(z) J_{n+1}(k_m r) + c_{n,m}^E(z) J_{n-1}(k_m r)] \exp(in\phi). \quad (\text{A16})$$

Equivalent equations are obtained for magnetic fields by substituting $c_n^E \rightarrow c_n^H$ and $b_n^E \rightarrow b_n^H$. The z components are obtained using the time-harmonic Maxwell's equations (A3) and (A6), the above expansions, and the derivation rules for Bessel functions as

$$i\omega\mu_0 H_{z,n} = \sum_{m=1}^M k_m^2 \Delta k_m [b_{n,m}^E - c_{n,m}^E] J_n(k_m r), \quad (\text{A17})$$

$$-i\omega\epsilon(r) E_{z,n} = \sum_{m=1}^M k_m^2 \Delta k_m [b_{n,m}^H - c_{n,m}^H] J_n(k_m r). \quad (\text{A18})$$

To obtain expression for $E_{z,n}(r)$, we expand Eq. (A18) using $E_{z,n} = \sum_{m=1}^M k_m \Delta k_m E_{z,n,m} J_n(k_m r)$, integrate both sides of Eq. (A18) with $\int_{r=0}^{\infty} r J_n(k_m' r) dr$, and use the orthogonality of the Bessel functions. We then obtain the expression for $E_{z,n,m}$, which is substituted to the expansion of $E_{z,n}$, giving

$$E_{z,n} = \frac{i}{\omega} \sum_{m,m'=1}^M ([\epsilon]_{m,m'}^{n,n})^{-1} k_{m'} [b_{n,m'}^H - c_{n,m'}^H] J_n(k_{m'} r), \quad (\text{A19})$$

where we have used the shorthand notation $[\epsilon]_{m,m'}^{n,n} = \int_{r=0}^{\infty} \epsilon(r) J_n(k_m r) J_n(k_{m'} r) r dr$.

The expansion coefficients b and c are obtained representing the system as an eigenvalue problem by applying the differential method as follows. The z dependence of the Maxwell's equations' expansion coefficients are written as an eigenvalue problem:

$$\frac{d\mathbf{f}_n(z)}{dz} = \mathbf{M}_n \mathbf{f}_n(z), \quad n \in [-N, N], \quad (\text{A20})$$

where $\mathbf{f} \in \mathbb{C}^{4M \times 1}$ and $\mathbf{M} \in \mathbb{C}^{4M \times 4M}$ are

$$\mathbf{f}_n(z) = \begin{bmatrix} b_{n,m}^E(z) \\ c_{n,m}^E(z) \\ b_{n,m}^H(z) \\ c_{n,m}^H(z) \end{bmatrix} \quad \mathbf{M}_n = \begin{bmatrix} M_{n,11} & M_{n,12} \\ M_{n,21} & M_{n,22} \end{bmatrix}. \quad (\text{A21})$$

Here the z dependence is of the form $\exp(i\beta z)$. The derivatives of the electric field expansion coefficients couple only to the magnetic field components and vice versa, so that the propagation constants β and expansion coefficients can be solved from the eigenvalue problem

$$-\beta_n^2 \begin{bmatrix} b_{n,m}^E \\ c_{n,m}^E \end{bmatrix} = M_{n,12} M_{n,21} \begin{bmatrix} b_{n,m}^E \\ c_{n,m}^E \end{bmatrix}. \quad (\text{A22})$$

The magnetic field expansion coefficients are obtained from the electric field ones using matrix $M_{n,21}$. Equivalently, the

eigenvalue problem can be written for magnetic field coefficients.

Derivating definitions in Eq. (A10) with respect to z , substituting Maxwell's Eqs. (A1)–(A6), and using the orthogonality of Bessel functions allows us to write

$$\frac{d\tilde{b}_{n,m}^E}{dz} = -\omega\mu_0\tilde{b}_{n,m}^H - \frac{k_m}{2\omega} \sum_{m'} ([\epsilon]_{m,m'}^{n,n})^{-1} k_{m'} [\tilde{b}_{n,m'}^H - \tilde{c}_{n,m'}^H], \quad (\text{A23})$$

$$\frac{d\tilde{c}_{n,m}^E}{dz} = -\omega\mu_0\tilde{c}_{n,m}^H - \frac{k_m}{2\omega} \sum_{m'} ([\epsilon]_{m,m'}^{n,n})^{-1} k_{m'} [\tilde{b}_{n,m'}^H - \tilde{c}_{n,m'}^H], \quad (\text{A24})$$

for the electric field coefficients and

$$\begin{aligned} \frac{d\tilde{b}_{n,m}^H}{dz} &= \frac{k_m^2}{2\omega\mu_0} (\tilde{b}_{n,m}^E - \tilde{c}_{n,m}^E) \\ &+ i\frac{1}{2}\omega k_m \int_{r=0}^{\infty} \epsilon(r) E_{r,n}(r) J_{n+1}(k_m r) r dr \\ &- \frac{1}{2}\omega k_m \int_{r=0}^{\infty} \epsilon(r) E_{\phi,n}(r) J_{n+1}(k_m r) r dr, \end{aligned} \quad (\text{A25})$$

$$\begin{aligned} \frac{d\tilde{c}_{n,m}^H}{dz} &= \frac{k_m^2}{2\omega\mu_0} (\tilde{b}_{n,m}^E - \tilde{c}_{n,m}^E) \\ &+ i\frac{1}{2}\omega k_m \int_{r=0}^{\infty} \epsilon(r) E_{r,n}(r) J_{n-1}(k_m r) r dr \\ &+ \frac{1}{2}\omega k_m \int_{r=0}^{\infty} \epsilon(r) E_{\phi,n}(r) J_{n-1}(k_m r) r dr, \end{aligned} \quad (\text{A26})$$

for the magnetic the field coefficients, where $\tilde{b}_{n,m}^E = k_m b_{n,m}^E$ and so on. The integrals in Eqs. (A25) and (A26) involving $E_{\phi,n}(r)$ can be calculated using the direct rule [30,31] as

$$\begin{aligned} &\int_0^{\infty} \epsilon(r) E_{\phi,n}(r) J_{n\pm 1}(k_m r) r dr \\ &= \sum_{m'=1}^M k_{m'} \Delta k_{m'} ([\epsilon]_{m,m'}^{n\pm 1, n\pm 1} b_{n,m'}^E + [\epsilon]_{m,m'}^{n\pm 1, n-1} c_{n,m'}^E), \end{aligned} \quad (\text{A27})$$

while the integrals involving $E_{r,n}(r)$ are calculated using the inverse rule due to the discontinuities of $\epsilon(r)$ and $E_{r,n}(r)$ as follows: The electric field can be expanded using the electric displacement as $E_{r,n}(r) = \sum_m k_m \Delta k_m \frac{1}{\epsilon(r)} D_{r,n,m}^{\pm} J_{n\pm 1}(k_m r)$, which has expansion components given by $E_{r,n,m}^{\pm} = \int_0^{\infty} E_{r,n}(r) J_{n\pm 1}(k_m r) r dr$ so that

$$\begin{aligned} E_{r,n,m'}^{\pm} &= \int_0^{\infty} E_{r,n}(r) J_{n\pm 1}(k_m r) r dr \\ &= \sum_m k_m \Delta k_m D_{r,n,m}^{\pm} \left[\frac{1}{\epsilon} \right]_{m',m}^{n\pm 1, n\pm 1}. \end{aligned} \quad (\text{A28})$$

The expansion for electric displacement is obtained by inverting as

$$D_{r,n,m}^{\pm} = \sum_{m'} \frac{1}{k_m \Delta k_m} \left(\left[\frac{1}{\epsilon} \right]_{m,m'}^{n\pm 1, n\pm 1} \right)^{-1} E_{r,n,m'}^{\pm}. \quad (\text{A29})$$

Solving $E_{r,n,m'}^{\pm}$ using Eq. (A15) and substituting into Eq. (A29) leads to

$$\begin{aligned} i k_m D_{r,n,m}^+ &= - \sum_{m'=1}^M \frac{1}{k_{m'} \Delta k_{m'}} \left(\left[\frac{1}{\epsilon} \right]_{m,m'}^{n+1, n+1} \right)^{-1} k_{m'} b_{n,m'}^E \\ &+ \sum_{m',m''=1}^M \frac{1}{k_{m'} \Delta k_{m'}} \left(\left[\frac{1}{\epsilon} \right]_{m,m'}^{n+1, n+1} \right)^{-1} \\ &\times k_{m'} \Delta k_{m''} [\Psi]_{m',m''}^{n+1, n-1} k_{m''} c_{n,m''}^E, \end{aligned} \quad (\text{A30})$$

$$\begin{aligned} i k_m D_{r,n,m}^- &= - \sum_{m',m''=1}^M \frac{1}{k_{m'} \Delta k_{m'}} \left(\left[\frac{1}{\epsilon} \right]_{m,m'}^{n-1, n-1} \right)^{-1} \\ &\times k_{m'} \Delta k_{m''} [\Psi]_{m',m''}^{n-1, n+1} k_{m''} b_{n,m''}^E \\ &+ \sum_{m'=1}^M \frac{1}{k_{m'} \Delta k_{m'}} \left(\left[\frac{1}{\epsilon} \right]_{m,m'}^{n-1, n-1} \right)^{-1} k_{m'} c_{n,m'}^E, \end{aligned} \quad (\text{A31})$$

where the following notations were used:

$$\left[\frac{1}{\epsilon} \right]_{m,m'}^{n,n} = \int_{r=0}^{\infty} \frac{1}{\epsilon(r)} J_n(k_m r) J_n(k_{m'} r) r dr, \quad (\text{A32})$$

$$[\Psi]_{m,m'}^{n\pm 1, n\mp 1} = \int_{r=0}^{\infty} J_{n\pm 1}(k_m r) J_{n\mp 1}(k_{m'} r) r dr. \quad (\text{A33})$$

Funding. European Metrology Research Programme (EMRP) (EXL02); Danish Research Council for Technology and Production (DFF-4005-00370); Villum Fonden.

Acknowledgment. This work was funded by project SIQUTE (contract EXL02) of the European Metrology Research Programme (EMRP). The EMRP is jointly funded by the EMRP participating countries within EURAMET and the European Union. Furthermore, support from the Danish Research Council for Technology and Production via the Sapere Aude project LOQIT (DFF-4005-00370), and support from the Villum Foundation via the VKR Centre of Excellence NATEC are gratefully acknowledged.

REFERENCES

1. K. J. Vahala, "Optical microcavities," *Nature* **424**, 839–846 (2003).
2. G. Lecamp, P. Lalanne, and J. P. Hugonin, "Very large spontaneous-emission β factors in photonic-crystal waveguides," *Phys. Rev. Lett.* **99**, 023902 (2007).
3. V. S. C. Manga Rao and S. Hughes, "Single quantum-dot Purcell factor and β factor in a photonic crystal waveguide," *Phys. Rev. B* **75**, 205437 (2007).
4. S. Strauf and F. Jahnke, "Single quantum dot nanolaser," *Laser Photon. Rev.* **5**, 607–633 (2011).
5. N. Gregersen, P. Kaer, and J. Mørk, "Modeling and design of high-efficiency single-photon sources," *IEEE J. Sel. Top. Quantum Electron.* **19**, 1–16 (2013).
6. A. V. Lavrinenko, J. Lægsgaard, N. Gregersen, F. Schmidt, and T. Søndergaard, *Numerical Methods in Photonics* (CRC Press, 2014), Chap. 7, pp. 197–249.
7. A. Taflov, *Computational Electrodynamics: The Finite-difference Time-domain Method, Antennas and Propagation Library* (Artech, 1995).

8. J. Reddy, *An Introduction to the Finite Element Method* (McGraw-Hill, 2005).
9. J.-P. Berenger, "A perfectly matched layer for the absorption of electromagnetic waves," *J. Comput. Phys.* **114**, 185–200 (1994).
10. E. Noponen and J. Turunen, "Eigenmode method for electromagnetic synthesis of diffractive elements with three-dimensional profiles," *J. Opt. Soc. Am. A* **11**, 2494–2502 (1994).
11. M. G. Moharam, E. B. Grann, D. A. Pommet, and T. K. Gaylord, "Formulation for stable and efficient implementation of the rigorous coupled-wave analysis of binary gratings," *J. Opt. Soc. Am. A* **12**, 1068–1076 (1995).
12. J. P. Hugonin and P. Lalanne, "Perfectly matched layers as nonlinear coordinate transforms: a generalized formalization," *J. Opt. Soc. Am. A* **22**, 1844–1849 (2005).
13. N. Gregersen, S. Reitzenstein, C. Kistner, M. Strauss, C. Schneider, S. Höfling, L. Worschech, A. Forchel, T. Nielsen, J. Mørk, and J.-M. Gérard, "Numerical and experimental study of the Q factor of high-Q micropillar cavities," *IEEE J. Quantum Electron.* **46**, 1470–1483 (2010).
14. M. Pisarenco, J. Maubach, I. Setija, and R. Mattheij, "Aperiodic Fourier modal method in contrast-field formulation for simulation of scattering from finite structures," *J. Opt. Soc. Am. A* **27**, 2423–2431 (2010).
15. P. T. Kristensen, C. V. Vlack, and S. Hughes, "Generalized effective mode volume for leaky optical cavities," *Opt. Lett.* **37**, 1649–1651 (2012).
16. J. R. de Lasson, "Modeling and simulations of light emission and propagation in open nanophotonic systems," Ph.D. thesis (Technical University of Denmark, 2015), available at http://orbit.dtu.dk/files/119895633/PhDThesis_Jakobrdl_Oct2015.pdf.
17. B. Guizal, D. Barchiesi, and D. Felbacq, "Electromagnetic beam diffraction by a finite lamellar structure: an aperiodic coupled-wave method," *J. Opt. Soc. Am. A* **20**, 2274–2280 (2003).
18. N. Bonod, E. Popov, and M. Nevière, "Differential theory of diffraction by finite cylindrical objects," *J. Opt. Soc. Am. A* **22**, 481–490 (2005).
19. G. P. Bava, P. Debernardi, and L. Fratta, "Three-dimensional model for vectorial fields in vertical-cavity surface-emitting lasers," *Phys. Rev. A* **63**, 023816 (2001).
20. M. Dems, I.-S. Chung, P. Nyakas, S. Bischoff, and K. Panajotov, "Numerical methods for modeling photonic-crystal VCSELs," *Opt. Express* **18**, 16042–16054 (2010).
21. J. Claudon, N. Gregersen, P. Lalanne, and J.-M. Gérard, "Harnessing light with photonic nanowires: fundamentals and applications to quantum optics," *ChemPhysChem* **14**, 2393–2402 (2013).
22. I. Friedler, P. Lalanne, J. P. Hugonin, J. Claudon, J. M. Gérard, A. Beveratos, and I. Robert-Philip, "Efficient photonic mirrors for semiconductor nanowires," *Opt. Lett.* **33**, 2635–2637 (2008).
23. L. Li, "Formulation and comparison of two recursive matrix algorithms for modeling layered diffraction gratings," *J. Opt. Soc. Am. A* **13**, 1024–1035 (1996).
24. A. V. Lavrinenko, J. Lægsgaard, N. Gregersen, F. Schmidt, and T. Søndergaard, *Numerical Methods in Photonics* (CRC Press, 2014), Chap. 6, pp. 139–195.
25. A. W. Snyder and J. D. Love, *Optical Waveguide Theory* (Chapman and Hall, 1983).
26. L. Novotny and B. Hecht, *Principles of Nano-Optics*, 2nd ed. (Cambridge University, 2012), Chap. 8, pp. 224–281.
27. J. R. de Lasson, T. Christensen, J. Mørk, and N. Gregersen, "Modeling of cavities using the analytic modal method and an open geometry formalism," *J. Opt. Soc. Am. A* **29**, 1237–1246 (2012).
28. J. P. Boyd, *Chebyshev and Fourier Spectral Methods*, 2nd ed. (Dover, 2001).
29. L. Novotny and B. Hecht, *Principles of Nano-Optics*, 2nd ed. (Cambridge University, 2012), Chap. 10, pp. 313–337.
30. L. Li, "Use of Fourier series in the analysis of discontinuous periodic structures," *J. Opt. Soc. Am. A* **13**, 1870–1876 (1996).
31. E. Popov, M. Nevière, and N. Bonod, "Factorization of products of discontinuous functions applied to Fourier-Bessel basis," *J. Opt. Soc. Am. A* **21**, 46–52 (2004).